

Stereo observation of lakes and coastal zones using ASTER imagery

John Matthews

COE Research Program, Department of Geophysics, Kyoto University, Kyoto 606-8502, Japan

Received 5 October 2004; received in revised form 26 April 2005; accepted 28 April 2005

Abstract

One of the unique features of the visible and near-infrared (VNIR) subsystem of the Advanced Spaceborne Thermal Emission and Reflection Radiometer (ASTER) is the near-infrared back-looking view, which is obtained 55 s later than the corresponding nadir view. Although the stereoscopic capability derived from a combination of these two views was originally designed for use in land applications, serendipitous observation has shown that it also represents a promising source of data over water bodies. In fact, when coupled with surface temperature measurements derived from the sensor's thermal-infrared (TIR) component, stereo viewing forms a powerful observational capability that can be exploited in the monitoring of lake and marine environments. One important aspect introduced by the stereo system is the capability to measure the short-term displacements associated with surface currents and waves by comparing the nadir and back-looking views. In initial results presented here, surface motion was deduced from the displacement of a ship wake appearing in the Sun glitter regime of an ASTER image of the Izu Shoto islands, which lie to the southwest of Tokyo Bay, Japan. Within the natural limitations imposed by spatial and temporal resolutions, this measurement was found to be consistent with simultaneous surface current values derived from a nearby shore-based High-frequency (HF) radar system. The success of this basic comparison introduces the possibility that stereo imaging from space, if well tuned to follow the motion of surface slicks and other surface features within the Sun glitter regime, could provide a future means of observing surface current on a global scale.

Data from the VNIR stereo system also highlights the influence of observational geometry. In the case of a surface with Sun glitter, this often manifests as a brightness reversal between the nadir and back-looking views in which relatively bright (dark) features at nadir appear dark (bright) in the back-looking view. Such a region of brightness reversal (ROBR) can be indicative of a locally rough or smooth surface texture as may be found, for example, in the vicinity of internal waves (rough) or ship wakes (smooth). Simple analysis based on a "Back to Nadir" ratio of relative radiances shows that the signal strengths measured by ASTER within a ROBR can yield a crude estimate of the mean square surface slope, which is an important parameter in theories of sea surface roughness imaging by devices such as Synthetic Aperture Radar (SAR).

Several other potential applications of VNIR stereo data in coastal zone and lake monitoring are considered here, including the study of internal waves (in the Strait of Gibraltar), derivation of wind velocity at cloud height, swell-wave propagation, suspended sediment transport, marine traffic monitoring and ship wake patterns. As the reflectivity of water in the near infrared reverses from low to high in the presence of Sun glitter, most of the applications discussed here involve glitter and hence some discussion of the influence of sensor view geometry is presented. The general conclusion of the paper is that future missions such as the Advanced Land Observing Satellite (ALOS), which aim to deploy high spatial resolution stereo viewing systems primarily for land applications, should also return data of considerable value in oceanography and limnology, particularly if their observational geometry can be adjusted to permit the imaging of Sun glitter from water surfaces.

© 2005 Elsevier Inc. All rights reserved.

Keywords: Stereo view; ASTER; Lakes; Coastal zones

1. Introduction

An innovative feature of the VNIR component of the Advanced Spaceborne Thermal Emission and Reflection Radiometer (ASTER) (Yamaguchi et al., 1998) is its ability

to acquire stereo data, in which regions are imaged first in channel 3N at nadir and then from channel 3B, a back-looking slant view obtained 55 s later. These two channels are identical in both bandwidth (0.78–0.86 μm in the near infrared) and spatial resolution (15 m). The stereo imaging mode was originally designed for digital terrain modeling in support of the terrestrial sciences (Yamaguchi et al., 1998)

E-mail address: johnp-matthews@hotmail.com.

and hence usually generates back-looking views at “Normal” gain levels to image relatively reflective land surfaces. Although the nominal gain setting and near-infrared wavelength used for this subsystem are not optimal for use over water, images derived from channel 3B over water do, in fact, contain much useful information. The present paper is therefore concerned with the use of ASTER’s stereo imagery in the study of *water* bodies such as lakes and inland seas and should compliment other aquatic applications of ASTER data that make principal use of the multi-band nadir views (Abrams et al., 2002).

The design of ASTER was not optimized for observation of water bodies. There is no blue channel, a wavelength at which penetration is good in clear water and at which phytoplankton strongly absorbs. In addition, the channel bandwidths of between 60 and 80 μm are relatively broad (compare to 20- μm widths for the Sea-viewing Wide Field-of-view Sensor (SEAWIFS) channels), which makes the development of algorithms for the retrieval of suspended sediment or phytoplankton more difficult. For sound reasons, from the perspective of geological remote sensing, ASTER uses six bands in the short wave-infrared (SWIR), but these channels deliver little extra information for observations within water bodies. However, the situation is not all bad since ASTER images gathered over water frequently contain areas of Sun glitter for which these deficiencies diminish in importance. Indeed, in the Sun glitter case, other aspects of ASTER such as the sensor tilt capability, the high spatial resolution of 15 m, simultaneous surface temperature measurement in the thermal infrared and, not least, the back-looking view from channel 3B, lend the instrument considerable potential for aquatic remote sensing.

As Sun glitter involves the direct reflection of sunlight from the water surface, rather than its penetration into the water column, the presence of glitter in an image is often considered to represent a serious data loss. For sensors with a variable viewing capability, careful mission planning in which appropriate values of the sensor tilt angle are employed (Mohan & Chauhan, 2001) can reduce the effect. Conversely, the acquisition of imagery containing areas dominated by Sun glitter can, in certain cases, be of great value (Khattak et al., 1991). This is particularly the case for the study of phenomena that influence the roughness of the water surface and which in turn modulate the reflected glitter intensity. For the obvious case of wind-induced surface roughness, the pioneering work of Cox and Munk (1954) led to the development of a well-known mathematical relation between the Sun glitter radiance detected within a specified viewing geometry and the surface wind speed. Later studies employed Sun glitter imagery in the study of features such as oceanic internal waves (Zheng et al., 1995), shallow water bottom topography (Hennings et al., 1994) and frontal boundaries (Matthews et al., 1997). In these latter cases, surface roughness change generally refers to variations in the amplitude of small-scale gravity waves and capillary waves. It is brought about in a number of ways,

such as through modifications to the water flow pattern, the development of surface slicks or breaking waves.

Visible-band images acquired in the normal (non-glitter) mode provide rather limited information on the dynamical properties of water bodies (such as waves or currents) due, in part, to the low intrinsic reflectivity of water. When Sun glitter is present, however, water surfaces often appear brighter than the adjacent land surfaces. The similarity of Sun glitter patterns to the Normalized Radar Cross Section (NRCS) modulations observed in Synthetic Aperture Radar (SAR) images of water bodies has fostered interest in the former as an aid to the interpretation of SAR. In general, however, there has been a tendency for remote-sensing scientists to employ SAR when making high spatial resolution studies of the dynamical aspects (such as waves or currents) of coastal regions or lakes. As a result, much of the potential of Sun glitter imagery has remained untapped. In this respect, the acquisition of a back-looking view in channel 3B of ASTER is significant for two main reasons. Firstly, it supplies a revisit image taken 55 s after the nadir view and so provides a means of measuring the spatial displacement associated with surface current and also generates a view of short-term variability. In addition, the slant image is gathered under a new observational geometry. When Sun glitter dominates, this enables crude estimates of an important surface roughness parameter – the mean square surface slope – to be made. The latter can be used to strengthen the interpretation of Sun glitter and SAR images since both essentially mirror the small-scale surface roughness variability of the water surface.

Particular emphasis is placed here on the study of internal waves using the ASTER stereo imaging system. Application of this new investigative technique to the study of this phenomenon probably represents the latest step in a well-established tradition that has employed optical remote sensing to good effect in internal wave research. This approach started early (Apel et al., 1975) and continues up to the present within the Land Remote Sensing Satellite (LANDSAT) and SPOT programs. In addition, many years of manned space flight missions have accumulated a considerable body of photographic material, some of which displays internal waves. The Sun glitter changes caused by internal waves are conventionally interpreted as resulting from the marshalling effect of their current gradient systems. These serve to modulate the small-scale surface roughness, so that an internal wave packet is generally represented by a series of alternate rough and smooth bands. The current systems may also concentrate local surfactant material into slicks that in turn cause wave damping. A more detailed assessment of this complex surface interaction is now becoming possible through data supplied by new instruments such as (the Medium Resolution Imaging Spectrometer (MERIS), which acquires multi-band data at a spatial resolution of 300 m (da Silva et al., 2004). High spatial resolution stereo data acquired by ASTER can also make a valuable contribution to this research effort.

The material presented in this contribution is arranged in the following order. Following a brief discussion of the geometry of Sun glitter observation, the paper discusses the use of stereo images in defining relative displacements that take place over the 55-s time delay between the nadir and back-looking views. This aspect has a number of obvious potential marine applications such as the measurement of surface current, ship traffic monitoring and the derivation of a cloud-height wind velocity. Here a surface current determination derived from an ASTER image of the northern Izu Shoto Islands (Japan) is compared with simultaneous surface current values measured by a coastal HF radar system operating on the adjacent mainland.

The paper then considers the appearances of specific oceanic features as recorded in the stereo view. Regions of brightness reversal (ROBRs) associated with strong internal waves and a ship wake are prominent in the Izu Shoto image. The internal waves, for example, appear dark in the near-nadir view and bright in the back-looking view. This reversal can be explained by considering the dependence of the received Sun glitter radiance on observational geometry and, through the use of a “Back to Nadir” ratioing method, can be used to derive a simple estimate of local mean square surface slopes when Sun glitter is dominant in both views.

A study of ASTER images of internal waves in the Strait of Gibraltar is then presented. In contrast to the Izu Shoto data, bright internal waves now appear in both the nadir and back-looking views. Again, consideration of the observational geometry and the local wind conditions leads to an understanding of the appearance of the internal waves and provides further estimates of the local mean square surface slope. The powerful observational capability offered by the tandem operation of ASTER with the Landsat Enhanced Thematic Mapper (ETM), in which the ETM gathers data some 41 min prior to ASTER, enables the motion of the internal waves at Gibraltar to be effectively tracked and provides a standard against which the quality of the measurements of internal wave motion derived from the ASTER stereo technique can be assessed.

In the final section, a number of other potential marine and lake applications of the stereo technique are very briefly considered. These include the imaging of swell waves, studies of suspended sediment transport and ship wakes. The summary considers the oceanographic potential of the forthcoming ALOS mission (which includes the Panchromatic Remote-sensing Instruments for Stereo Mapping (PRISM) sensor) in the context of more general requirements for a space-borne sensor dedicated to the stereo observation of water surfaces.

2. Sun-glitter geometry in the back-looking view

In order to form a basis for the interpretation of stereo images of limnological and oceanographic phenomena, it

is first necessary to identify the influence of the new geometry associated with the back-looking view. This discussion is aimed primarily towards the case of an ocean surface covered by Sun glitter, since this plays an important facilitating role in highlighting the surface structures of water bodies. At the near-infrared wavelength employed for ASTER’s stereo view, a glitter-free sea surface would generally appear dark and relatively featureless.

Consider the TERRA host satellite to be traveling from north to south along an orbital path that lies parallel to the y -axis of Fig. 1. In the near-nadir looking configuration, the ASTER sensor views at an incidence angle θ along the x -axis towards a wave facet on the water surface that is located at the origin. The solar zenith and azimuth angles are ζ and Φ , respectively. For Sun glitter, the wave facet must tilt at an angle β_{sg} in order to cause direct reflection of the incident sunlight into the sensor. The corresponding angle of reflection is ω_{sg} and simple geometry shows that

$$\cos(2\omega_{sg}) = \cos\theta\cos\zeta - \sin\theta\sin\zeta\sin\Phi \quad (1)$$

or, in the case that the host satellite travels along a path that is oriented away from a north-south line by an azimuth angle τ , then Eq. (1) is modified as

$$\cos(2\omega_{sg}) = \cos\theta\cos\zeta + \sin\theta\sin\zeta\sin(\tau - \Phi). \quad (2)$$

The required tilt of the wave facet is obtained from the relation

$$\cos\beta_{sg} = (\cos\theta + \cos\zeta)/(2\cos\omega_{sg}). \quad (3)$$

These conditions are well known (Hennings et al., 1994). Consider now the situation for the back-looking view obtained by channel 3B of ASTER with a base-to-height ratio of 0.6 within the stereo image pair. The sensor looks towards the origin at a new value of the incidence angle

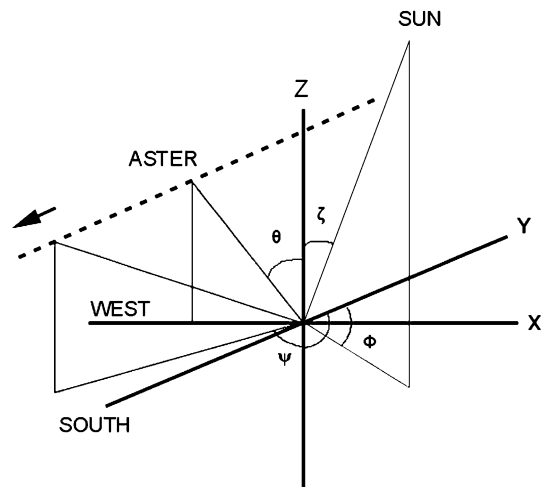


Fig. 1. Observational geometry for Sun glitter in ASTER stereo image pairs.

(labeled θ') and along an azimuth angle ψ . The relevant relations are derived here as

$$\cos(2\omega_{sg}) = \cos\theta' \cos\zeta + \sin\theta' \sin\zeta \cos(\psi + \tau - \Phi) \quad (4)$$

with

$$\psi = 270 - \tan^{-1}(0.6/\tan\theta) \quad (5)$$

and

$$\cos\beta_{sg} = (\cos\theta' + \cos\zeta)/(2\cos\omega_{sg}). \quad (6)$$

These additional equations dictate that considerably larger angles of tilt are required to produce a Sun glitter signature in the channel 3B back-looking view. Frequent reference to the results of this simple geometrical analysis will be made in the forthcoming material.

As a next step in the construction of a theoretical framework, it is possible to calculate glitter radiances for specified slope probability distribution functions of the reflecting facets. Melsheimer and Kwoh (2001) have presented work along these lines in their interpretation of images derived from the System Pour l'Observation de la Terre (SPOT) satellite for which, of course, a back-looking view was not available. The availability of the second (slant) view with ASTER, however, rather transforms the situation by enabling basic parameters relating to the small-scale roughness structure of the sea surface to be derived. Before turning to this aspect it is first necessary to discuss an example of the stereo imaging of a coastal region by ASTER in the Sun glitter regime and to highlight its most basic aquatic application - that of surface current measurement.

3. The measurement of surface current by comparing nadir and back-looking views

A weakness of present space-based observational techniques for water-body sensing is the inability to measure currents regularly, in synoptic fashion and at high spatial resolution. As ASTER is configured for land observation, the data it obtains do not offer a general solution to this problem but can provide surface current values under certain circumstances. In the absence of Sun glitter, this involves the straightforward measurement of the displacement of bright objects such as foam lines or artifacts of debris that are occasionally defined in both nadir and back-looking views. In general, however, this ideal situation is rarely encountered. On the other hand, when the ASTER sensor pointing angles are set in an appropriate direction, a more or less regular acquisition of Sun glitter images becomes possible. These images can reveal the subtle surface structure of the ocean (Munk et al., 2000). If the motion of such structures can be tracked across the time interval separating the two images gathered during stereo observation, then in principle this would form the basis for a new means of surface current

observation. The basic motivation for the work presented in this section lies in this concept.

Fig. 2a shows a portion of a stereo image acquired by ASTER of part of the Izu Shoto region east of the Izu peninsula (Japan) with the island of Toshima visible on the top right (island center 34.52°N, 139.279 E). These level 1A data were recorded at 01.39 UT (10.39 am Japan Standard Time, JST) on 19 June 2004 within band 3N (near-infrared, 0.78–0.86 μm) at the “High” gain setting of the VNIR subsystem. The pixel size here is 15 m. The corresponding back-looking view gained from channel 3B is shown in Fig. 2b and, unusually, was also collected at the “High” gain setting. These, and the subsequent images discussed in this article, are aligned in the orbital path orientation.

For the near-nadir data of Fig. 2a, the sea surface is largely covered by Sun glitter and appears bright. At the time of acquisition, the TERRA platform was following a descending path with the ASTER sensor viewing at an angle of 5.73° to the left so that images were collected from the sunward side of the spacecraft. The extract shown in Fig. 2a is taken from the outer (sunward) edge of the swath where the viewing angle nears 8.125°. For this time and observational geometry, Eq. (3) dictates that small tilts of value $\beta_{sg}=5.59^\circ$ in the orientation of local reflecting facets were sufficient to cause glitter. Solar radiation mirrored off the surface of the sea was then able to travel directly to the spacecraft without entering the water column. As a result, the ocean surface shown in Fig. 2a appears bright owing to the ubiquity of reflecting facets at the appropriate orientation. In contrast, glassy calm regions of water without Sun glitter (none are present in Fig. 2a) appear as dark zones due to the low intrinsic reflectivity of water. Note also that regions of higher small-scale surface roughness, such as are visible on the windward (south) side of Toshima and in the vicinity of strong internal waves (one example is indicated by the white arrow in the lower left of Fig. 2a), take on a darker appearance. As discussed below, this is because the surface slope probability distribution functions in these regions are less favorable for near-nadir Sun glitter within this geometry. The extensive bright line passing close to the west side of Toshima represents the wake created by a ship that is visible on the lower right quadrant as it steams on a southward heading. In addition, note that cloud shadows are well-defined in the image.

ASTER acquired the back-looking view of Fig. 2b from a slanted angle of incidence of 31.66° and 55 s later than the nadir view of Fig. 2a. From Eq. (6) the required angle of tilt (β_{sg}) for Sun glitter is now 19.96°. Here, with a lower overall glitter contribution, the image is generally darker as glitter-free water columns reflect little at this near-infrared wavelength. Nevertheless, it is possible to identify many of the surface features present in the nadir view, except that now these often appear reversed in relative brightness. Similar brightness reversals have been identified in earlier studies (Hennings et al., 1994; Matthews et al., 2004). In the Fig. 2 stereo pair, particularly clear reversals are associated with the internal waves (dark near nadir changing to bright in the

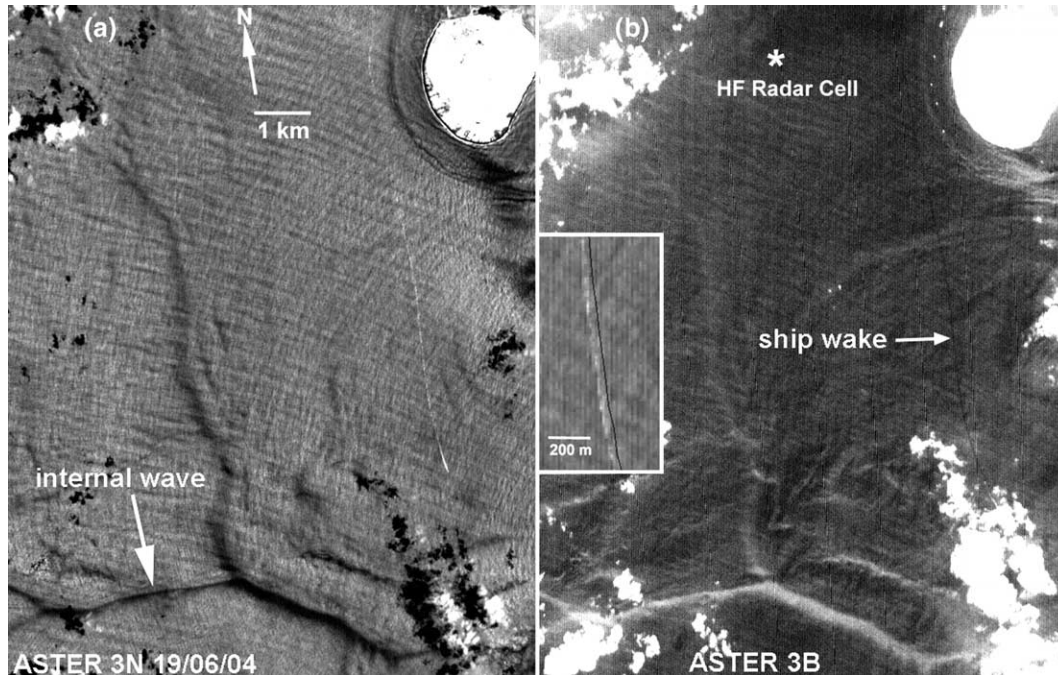


Fig. 2. (a) A portion of an ASTER channel 3N (near-infrared) image of the Izu Shoto region east of the Izu peninsula near Toshima Island (center 34.52° N, 139.279° E), which appears on the top right of the image. These data were acquired using a pointing angle of 5.729° and a “High” gain setting on 19 June 2004 at 01.39 UT (10.39 am JST). The white arrow (lower left) marks a portion of a strong internal wave. A ship and its bright wake are clearly visible to the south of the island. Cloud shadows and swell waves are well defined. (b) ASTER channel 3B (near infrared) data corresponding to the area shown in (a). This image was gathered 55 s later from a back-looking slant view and using a “High” gain setting. The star-shaped symbol near the top of the image denotes the center point of a nearby HF radar cell from which surface current was measured at 09:00 am JST. The white arrow (right of center) indicates the position of the ship wake shown in (a), which has now become dark in appearance. In contrast, the internal wave has become bright. The small image inserted on the left shows in detail the eastward displacement of the ship wake over the 55-s time delay between the 3N and 3B views. Here the position of the ship wake derived from the slant view (outlined in black) is traced onto a small extract from the nadir view.

back-looking view) and with the ship wake (bright to dark), which is marked by a white arrow in Fig. 2b. Reflection by foam in the ship wake is not involved here, as this would produce bright returns in both views.

Careful co-registration of the images in the stereo pair then enables surface motion to be determined from the differential displacement within the ROBR. Clearly, to be detectable, the current must produce a shift in excess of 1 pixel over the 55 s temporal separation between the two images, which corresponds to a minimum speed of 0.27 m s^{-1} . The small vignette in Fig. 2b shows an expanded view of the ship wake as imaged in channel 3N together with the traced centerline of the wake recorded in the back-looking slant view of channel 3B. Within a nominal accuracy of ± 1 pixel, the displacement due to the surface motion measured here amounts to 2 pixels, and thus corresponds to an eastward current of 0.54 m s^{-1} , with the speed tending to increase in the close vicinity of the island. In a similar fashion, wind velocity at cloud height can be directly determined from the motion of cloud shadows across the sea surface (Takasaki et al., 1994). In channel 3B the cloud shadows are less obvious than at nadir but nevertheless can still be identified through careful image processing. In this case the tracking procedure yields a cloud-height wind speed of about 6 m s^{-1} (a Force-4 moderate breeze), blowing in a southwesterly direction. The VNIR spatial resolution of 15 m inevitably quantizes the measure-

ments of surface displacement and will adversely affect the determination of low velocities associated with water motion in particular.

Note that the values of current obtained in this way are derived from direct assessments of spatial translation and do not rely on secondary effects such as the number of revolutions made by current meter rotors. Moreover, as they represent true surface motion inclusive of all effects such as local wind forcing and of wave-induced Stokes drift, they will differ from surface currents derived on the basis of ocean circulation models. As conventional instrumentation such as current meters and Acoustic Doppler Current Profilers return data beyond minimum depths of a few meters, the closest counterpart to the surface measurement made here is the current derived by coastal HF radar remote sensing, since this refers to the top few centimeters of the water column.

Originally Crombie (1955) discovered that the two peaks present in HF-radar sea echoes (which result from Bragg scattering by approaching and receding gravity wave fields) are slightly displaced away from a position of symmetry within the Doppler spectrum by an underlying current. This observation formed the basis of future operational shore-based radar systems for measuring coastal circulation (Barrick et al., 1977). Further validation of the HF radar remote-sensing technique (Prandle & Ryder, 1985) led to a greater level of acceptance by the oceanographic community

and to subsequent applications within dedicated oceanographic research programs (Matthews et al., 1993; Prandle & Matthews, 1990). Here data derived from a nearby operational HF radar system are used to verify the surface current determination derived from the ASTER stereo image of the Izu Shoto region.

Surface currents were obtained from a 5 MHz HF radar operated by the Japan Coast Guard, which transmits on a regular basis from stations at Hachijojima and Nojima. The system maps a large swath of ocean, covering the approaches to Tokyo Bay and much of the Izu Shoto island region, at a nominal spatial resolution of 10 km (Kinoshita et al., 2004). On the date of acquisition of the image shown in Fig. 2 (19 June 2004), this radar provided synoptic surface current maps at 09.00 and 12.00 JST. The HF radar cell closest to the ship wake shown in Fig. 2 is located at 34.53° N, 139.22° E and is labeled near the top of Fig. 2b. At 09.00 JST a surface current speed of 0.38 m s⁻¹ was measured at this point flowing in a direction of 82° with respect to north. Largely eastward flows of very similar magnitude were recorded at all other nearby cells. At the later time of 12.00 JST, the nearest cell point was located just to the north of Toshima (not visible in Fig. 2) at 34.62° N, 139.22° E, and here a current speed of 0.54 m s⁻¹ flowing at 77° with respect to north was recorded. Motion in a generally eastward direction and at a similar speed was once more measured at other nearby HF radar intersection points.

These values can be compared with the surface speed of 0.54 m s⁻¹ implied by the two-pixel eastward displacement of the ROBR associated with the ship wake in Fig. 2, which corresponds to the situation at 10.39 JST. Within the constraints imposed by the spatial resolution of the VNIR instrument and the temporal resolution of the HF radar system, this comparison indicates that the measurements of surface current obtained from these two sources are consistent at a basic level. A more rigorous statistical approach is clearly possible as a next step. Indeed, as the future accuracy of the surface current determinations based on stereo observation from space increases (principally through the use of sensors with higher spatial and radiometric resolution), it may then prove possible to make a very precise assessment of the accuracy and reliability of the HF radar technique under a wide variety of wind and tidal conditions.

The discussion presented in this section demonstrates that a stereo-viewing sensor would have considerable potential for surface current measurement if configured specifically for ocean surface observation. This would mainly require careful adjustment of the sensor-pointing angle (enabling it to image Sun-glitter), high sensitivity of operation in the back-looking view and a high spatial resolution of a few meters. In particular, if the system could be developed to track surface slicks, which are ubiquitous over large areas of the world's oceans, then the method might be applicable on a global scale. To illustrate this possibility, an image of surface slicks, derived from the 19

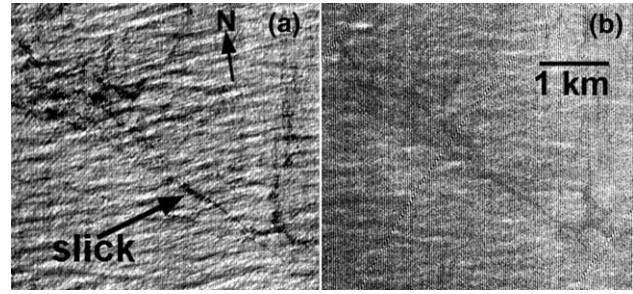


Fig. 3. (a) An enlarged image of surface slicks derived from Channel 3N of the 19 June 2004 ASTER scene of the Izu Shoto discussed in connection with Fig. 2. These features were located on the west side of the Izu peninsula near the inner edge of the ASTER swath. (b) The Channel 3B image corresponding to (a). Comparison of these two views shows that the slicks move in a north-northeastward direction at about 1 m s⁻¹.

June 2004 ASTER image of the Izu Shoto, is given in Fig. 3. These features were located on the west side of the Izu peninsula (near the inner edge of the ASTER swath) and hence unfortunately lie beyond the range of the HF radar operated by the Japan Coast Guard. Comparison of the near-nadir and back-looking views shows that the slicks move in a north-northeastward direction at about 1 m s⁻¹. The fact that both of these slicks are represented as relatively dark areas in the images will be discussed in the next section.

4. Estimation of the mean square surface slope

The Sun glitter radiances measured by ASTER in the near-nadir and back-looking views of Fig. 2 can be used to provide a quantitative measure of the roughness of the ocean surface at specific locations within an image. Since the method employed to do this makes use of a “Back to Nadir” ratio of relative radiances, it is well-suited to the investigation of the surface roughness qualities of ROBRs.

The Sun-glitter radiance L_{sg} measured by a sensor at an off-nadir pointing angle of θ° ($\theta^\circ < 80^\circ$) is given by (Zeisse, 1995)

$$L_{sg} = 0.25H_s p(z_{x,sg}, z_{y,sg}) \rho(\omega_{sg}) / (\cos^4 \beta_{sg} \cos \theta), \quad (7)$$

where H_s represents the incident solar irradiance, $z_{x,sg}$ and $z_{y,sg}$ are the x - and y -direction sea surface slopes required for specular reflection of sunlight directly back to the sensor, $p(z_x, z_y)$ signifies the surface slope probability distribution function and $\rho(\omega_{sg})$ represents the Fresnel reflection coefficient of the sea surface.

Making use of the relation $\tan^2 \beta_{sg} = (z_{x,sg})^2 + (z_{y,sg})^2$ and assuming a Gaussian form for $p(z_x, z_y)$ then gives

$$L_{sg} = 0.25H_s \rho(\omega_{sg}) \exp(-\tan^2 \beta_{sg} / \sigma^2) / (\pi \sigma^2 \cos^4 \beta_{sg} \cos \theta), \quad (8)$$

where σ^2 is the mean square surface slope. Melsheimer and Kwoh (2001) based their analysis of SPOT data on Eq. (8), the important aspect of which is the glitter radiance

maximum that develops at $\sigma^2 = \tan^2 \beta_{sg}$. For the near-nadir ASTER data of Fig. 2a, with $\beta_{sg} = 5.59^\circ$, this gives $\sigma^2 = 0.0096$, so that regions with mean square surface slope near to this value will appear bright in the image. Similarly, for the back-looking view of Fig. 2b, the maximum is at $\sigma^2 = 0.132$. This very high value implies that Sun glitter brightness in the slant view will gradually increase with small-scale surface roughness.

Consider now the ROBR associated with the internal wave observed in the Izu Shoto image for 19 June 2004 (this feature is labeled in Fig. 2a). Omitting the perturbation to the slope angle, the ratio N_{RR} of the glitter radiance received near nadir from within the region influenced by the internal wave field to that from the (nearby) unperturbed background is given by

$$N_{RR} = \left(\frac{\sigma_{CM}^2}{\sigma_{IW}^2} \right) \exp \left[\tan^2 \beta_{N.sg} \left(\sigma_{CM}^{-2} - \sigma_{IW}^{-2} \right) \right]. \quad (9)$$

Here σ_{CM} and σ_{IW} represent idealized mean square surface slopes corresponding to the ambient background and internal wave regions, respectively. The former is modeled through use of the Cox and Munk (CM, 1954) relation,

$$\sigma_{CM}^2 = 0.003 + 0.00512 S_w \pm 0.004, \quad (10)$$

with S_w symbolizing the near-surface wind speed in $m s^{-1}$.

Similarly, for Sun glitter within the back-looking view, the radiance ratio from within the region influenced by the internal wave field to that from the (nearby) unperturbed background is given by

$$B_{RR} = \left(\frac{\sigma_{CM}^2}{\sigma_{IW}^2} \right) \exp \left[\tan^2 \beta_{B.sg} \left(\sigma_{CM}^{-2} - \sigma_{IW}^{-2} \right) \right]. \quad (11)$$

Hence a ‘‘Back to Nadir’’ ratio of the relative radiances can be formed as

$$(B_{RR}/N_{RR}) = \exp \left[\left(\tan^2 \beta_{B.sg} - \tan^2 \beta_{N.sg} \right) \left(\sigma_{CM}^{-2} - \sigma_{IW}^{-2} \right) \right]. \quad (12)$$

This quantity is now equated to the ‘‘Back to Nadir’’ ratio that can be derived directly from the received ASTER radiances on the assumption that other (non-glitter) contributions to this ratio are small. When converted to radiance, measurements of digital number obtained from channels 3N and 3B on 19 June 2004 lead to the observed values of $B_{RR} = 1.26$ and $N_{RR} = 0.66$, so that the Back to Nadir relative radiance ratio becomes $(B_{RR}/N_{RR}) = 1.91$. Also the angles $\beta_{N.sg}$ and $\beta_{B.sg}$ are given from Eqs. (3) and (6) as 5.593° and 19.963° , respectively and hence

$$\left(\sigma_{CM}^{-2} - \sigma_{IW}^{-2} \right) = 5.288 \quad (13)$$

At this stage it is possible to insert this value of $(\sigma_{CM}^{-2} - \sigma_{IW}^{-2})$ into either Eqs. (9) or (11) and then solve for both σ_{CM}^{-2} and σ_{IW}^{-2} . However, a more realistic approach is adopted here by using Eq. (10) to define σ_{CM}^2 through the wind speed that was derived earlier from the motion of cloud shadows (given as $6 m s^{-1}$ at cloud height). For the purpose of this illustration, a simple ‘‘one seventh’’ power law is used to

project this wind speed to the surface. This approximation yields a value of $S_w = 2.2 m s^{-1}$, assuming the clouds to be at an altitude of about 1000 m, although the conclusions made below are not sensitive to the exact value of S_w within a sensible range. Inserting this value into Eq. (10) then gives a value for σ_{CM}^2 equal to 0.0143 so that σ_{IW}^2 becomes 0.0155, showing that the relative surface roughness increases within the region associated with the internal wave. Also, from the discussion following Eq. (8), as the value of σ_{CM}^2 is closer than that of σ_{IW}^2 to the value $\tan^2 \beta_{sg} = 0.0096$, corresponding to maximum glitter, it follows that the unperturbed background is brighter than the region within the internal wave. For the back-looking slant view, on the other hand, where the Sun glitter maximum occurs at much higher values of mean square surface slope, the fact that σ_{IW}^2 is greater than σ_{CM}^2 means that the internal wave should appear slightly brighter. As a result of these relative changes, the internal wave appears as a ROBR within the stereo image pair.

An identical procedure can be used to estimate the mean square surface slope within the region of the ship wake discussed in connection with Fig. 2. Now the opposite behavior is observed with $N_{RR} = 1.149$ and $B_{RR} = 0.913$, giving a ‘‘Back to Nadir’’ ratio of 0.795 so that

$$\left(\sigma_{CM}^{-2} - \sigma_{wake}^{-2} \right) = -1.879. \quad (14)$$

Using $\sigma_{CM}^2 = 0.0143$ as before, the derived value for σ_{wake}^2 (the mean square surface slope within the wake) becomes roughly 0.0139. This shows that the water surface within the wake is locally smoother than that in nearby undisturbed regions. It appears as a relatively bright line in the nadir images since σ_{wake}^2 is closer to the value of 0.0096 required for maximum Sun glitter radiance. Conversely, the wake appears as a dark line in the channel 3B slant view owing to its lower small-scale surface roughness (i.e. smoother surface). Hence, the ROBR formed in the case of the wake changes in the opposite sense to that associated with the internal wave.

The simple comparative approach outlined here is best used within limited areas for which the value of $\beta_{N.sg}$ remains essentially constant. To illustrate the danger involved when the theory is over-extended, consider that near the outer (sunward) edge of the Izu Shoto scene, the value of the surface tilt angle for Sun glitter is given by $\beta_{N.sg} = 5.59^\circ$ for the near-nadir view. However, the value of this parameter increases to $\beta_{N.sg} = 7.587^\circ$ near the inner edge of the swath, which lies nearly 60 km to the west. The value of $\tan^2 \beta_{N.sg}$ then becomes equal to 0.0177, which shifts the maximum in Sun glitter radiance to considerably higher mean square slopes, equivalent to higher small-scale surface roughness. As a result, a slick or wake region may be bright at the outer edge of the nadir scene whereas a similar feature located near the inner edge of the swath becomes quite dark. Within this inner region, the nadir image of the water surface then takes on an inverted or ‘‘flipped’’ appearance. At least for the Izu Shoto data, the above theory does not provide a fully quantitative description on a synoptic scale

when such major and rapid changes in brightness develop across the nadir scene. As the slicks shown in the 3N and 3B views of Fig. 3 are taken from near the inner edge of the swath, where the nadir brightness is inverted, both of these features appear dark.

In addition to improved modeling of the influence of changing scene geometry, the approach described here can be refined in several other ways, for example, by a better representation of the slope probability distribution function (Liu et al., 1997), accurate estimation (or measurement) of the surface wind and through inter-comparison with results from SAR images of the ocean surface. However, for some cases involving near-nadir glitter, the assumption that Sun glitter also dominates in the back-looking view becomes suspect when, for example, suspended sediment in estuarine regions makes a sizeable contribution to the radiance received in channel 3B.

5. Internal waves in the Strait of Gibraltar observed in stereo and tandem modes

The discussion now centers on the well-defined internal waves formed in the Strait of Gibraltar as imaged in stereo by ASTER on 5 July 2000 (Fig. 4(a–d)). Important supporting information is also derived from a LANDSAT Enhanced Thematic Mapper (ETM) scene acquired “in tandem” about 41 min earlier than the acquisition time of the ASTER image. In a largely comparative approach, frequent reference is made to the internal waves identified in connection with the Izu Shoto image and to the analysis of the previous section.

Within the area of the Strait of Gibraltar, warm, less saline Atlantic water moves eastward in an upper layer whereas below, a denser, more saline Mediterranean water component outflows westward. The internal waves develop at an interfacial depth of about 100 m as a tidal bore when diurnal tidal forcing relaxes over a shallow region called the Camarinal Sill, which lies further to the west of the area covered in the Figures. The pulses then propagate to the east in the form of well-defined wave packets, which gradually spread out geometrically and refract around bottom topography features. Internal waves at Gibraltar have been well-researched and their theoretical description has benefited from data supplied by a variety of observational techniques such as SAR (Brandt et al., 1996) and ground-based radar remote sensing (Watson & Robinson, 1990).

The level 1A ASTER data of Fig. 4 depict the situation to the east of the Strait at 11.29 UT on 5 July 2000, 53 min prior to springs low water (and roughly 5 h after high water). The images were acquired when the TERRA platform was in descending mode and the VNIR telescope was pointing at an angle of only 0.027° , implying almost nadir mapping. Both channels 3N and 3B were operating at “Normal” gain levels, in contrast to the Izu Shoto data shown in Fig. 2. For the channel 1 (green) nadir view of Fig.

4a, a main internal wave packet spans the width of the Strait in a distorted bow shape and is particularly well-defined in the southeast of the image. The Sun glitter variations highlight at least six individual wave fronts.

In addition to this main pulse, numerous other internal wave packets are also visible. Prominent amongst these is a group of two main waves (marked by the unlabelled white arrow) that lie roughly east of the image center and propagate in a range of directions between south and southeastward. These features appear to represent one arm of an oblique V-shaped disturbance, the apex of which is located further to the west. In all cases, variations in the Sun glitter intensity allow the individual wave components to be identified. A very similar representation of the internal wave field is offered by channel 3N, as presented in Fig. 4b. Sun glitter must also be involved at this wavelength because in its absence the sea surface would be uniformly dark. In both Fig. 4a and b, the signature of the main wave packet disappears toward the center of the channel (upper right quadrant). Note also that the extensive wake created by a large ship in the upper left quadrant of the image traverses the main wave group.

Using Eq. (3) within the observational geometry for the scene center, and neglecting slopes due to the amplitudes of the internal waves, a wave facet on the water surface must tilt at an angle of $\beta_{sg}=9.1^\circ$ in order to cause specular reflection of sunlight to the spacecraft. The maximum in glitter radiance therefore occurs at a value of $\sigma^2=\tan^2\beta_{sg}=0.0257$, which is considerably higher than for the Izu Shoto images. Meteorological observations made at Gibraltar at this time recorded a light easterly wind (Forces 1 to 3) and hence a mid-channel wind speed of 3 m s^{-1} is assumed here. From Eq. (10) this yields a value for σ_{CM}^2 , the mean square surface slope of the ambient background regions, of about 0.0184. As the dark areas (“troughs”) within the wave field are smaller in spatial width than the “crests” where enhanced glitter is present, this suggests an additive influence from the ambient background glitter due to merging and hence a corresponding value of N_{RR} , (measured at the internal wave “crests” relative to the background) that is very close to unity. For the troughs themselves, the suppression is evident within the nadir image and is expressed by $N_{RR, \text{trough}}=0.8$.

The internal waves associated with the main pulse and the V-shaped feature are also visible on the back-looking view derived from channel 3B (Fig. 4c), gathered 55 s later than the nadir images. The inferior quality of this image underlines the need for “High” gain settings for oceanographic applications. The view angle for this slant acquisition is now close to 31° and hence, from Eq. (6), the required tilt of a wave facet for specular reflection becomes 22.2° , showing once more that much greater mean square surface slopes (of value near 0.166) are required for maximum Sun glitter than at nadir. Measurement of the radiances at the crests gives $B_{RR}=1.1$ corresponding to a slight enhancement relative to the ambient background.

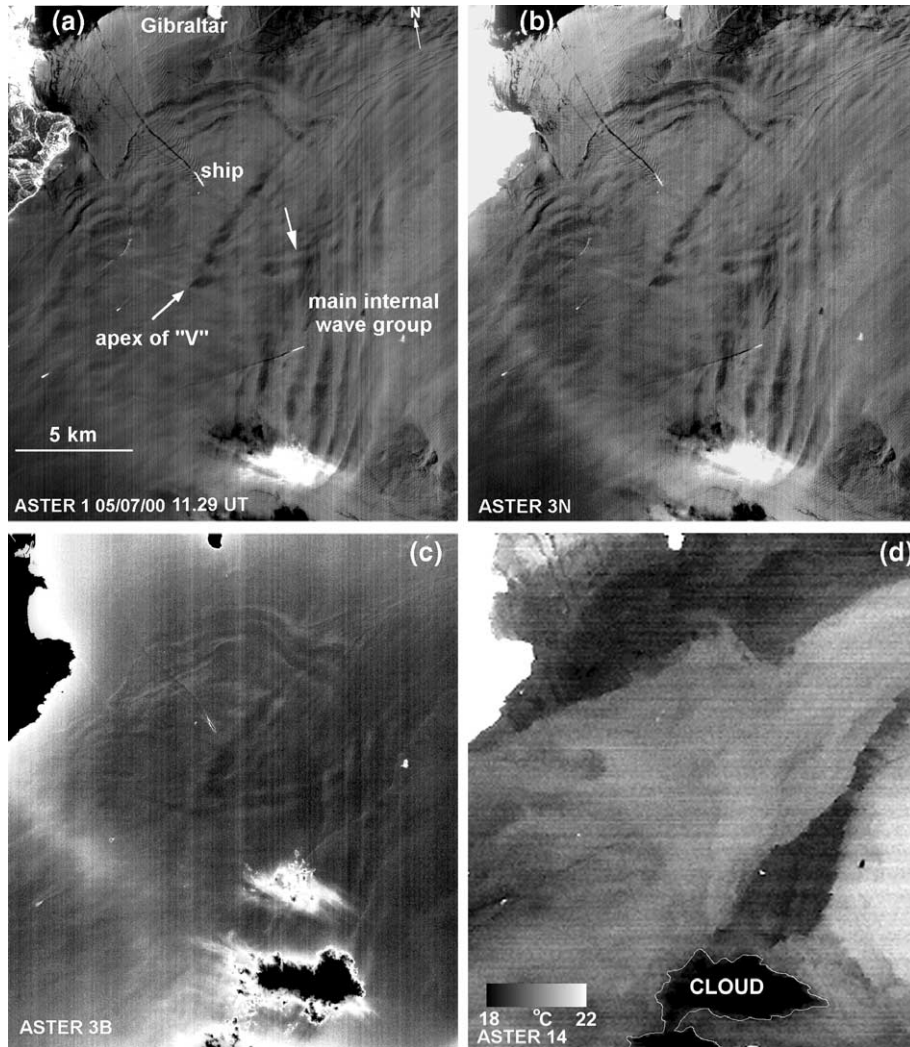


Fig. 4. (a) Data obtained in VNIR channel 1 (green) on 5 July 2000, depicting the region to the east of the Strait of Gibraltar at 11.29 UT. Sun glitter variations highlight a main internal wave packet that propagates eastward and spreads outwards. This feature consists of at least six waves that span the width of the Strait in a distorted bow shape. The individual waves are well-defined in the southeast of the image. In addition to this main pulse, a number of other internal wave packets are visible. A relatively strong group of two main waves lies roughly east of the image center (marked by the unlabelled arrow) and appears to be propagating south or southeastward. (b) The nadir view derived from channel 3N (near infrared) corresponding to the channel 1 data of (a). With the same observational geometry, the internal wave field highlighted in the Sun glitter variations is very similar to that observed in channel 1. In both (a) and (b), the main wave packet is suppressed towards the center of the channel (northeast quadrant). Note also the presence of a large ship steaming roughly southeastward in the northwest quadrant of both images. This vessel creates an extensive wake that traverses the main group of internal waves. (c) Internal waves are also visible in this slant image derived from channel 3B and gathered some 55 s later than the nadir data. The bright zones are somewhat narrower than in (a) and (b), showing that the appearance of the internal wave packet is influenced by the viewing geometry. (d) The corresponding TIR image is derived from Channel 14 of the TIR subsystem. These data provide a high-resolution view of sea surface temperature variation that shows a well-defined flow of warmer water passing northeastward and gradually narrowing in width as it moves into the Mediterranean. The disappearance of the internal waves from the images in the center channel region of the northeast quadrants of (a), (b) and (c) coincides with the narrowing and presumably strengthening of the flow in that region. Surface temperatures were calculated on the basis of the algorithm derived by Sakuno and Matsunaga (2002).

From the “Back to Nadir” ratio of Eq. (12), the mean square surface slope at the internal wave crests therefore becomes $\sigma_{IW}^2 = 0.0186$, which is slightly greater than that of the ambient background but is nevertheless well short of the value required for maximum nadir Sun glitter. The analogous computation for the troughs yields $\sigma_{IW, \text{trough}}^2 = 0.0179$, showing that these darker regions are locally smoother.

For the channel 3B image, the zones of higher surface roughness are slightly brighter and better defined whereas

now the smoother troughs tend to merge with the dark ambient background. As a result, the bright zones in the back-looking view are spatially narrower than in Fig. 4a and b, showing that the shape of the individual components within the internal wave packet is sensitive to view angle. In one sense this is unfortunate since it hinders the use of the stereo pair in deriving spatial displacements resulting from propagation of the internal wave fronts. Where the correspondence between the nadir and back-looking views remains good, attempts have been made to measure the

wave propagation speeds from the differential motion. However, at this spatial resolution and with a time interval of only 55 s separating the two images this task is not straightforward and the impression gained is one of a patchy variation in speed, with spatial displacement apparently well-defined at some points along the wave front and small or absent at others. This variability underlines the great advantage of ground-based radar in providing a temporal sequence of synoptic maps of surface backscatter that facilitates the identification of wave motion by the human eye.

It also highlights the value of operating missions such as ASTER and the LANDSAT ETM in a coordinated “tandem” mode in which they are able to image the same regions of the earth’s surface in close sequence. To illustrate this point, consider the ETM image depicted in Fig. 5. Here the data from channel 2 (green) of the ETM were acquired at 10.48 UT on 5 July 2000, just over 41 min prior to the TERRA overpass. As a result, the same internal wave field (which is again made visible through the Sun glitter intensity modulations it produces) is located westward of its position in the later ASTER image (traced in white). The speed of motion of the internal wave group can now be derived directly and is equal to 1.14 m s^{-1} in mid-channel and 0.47 m s^{-1} for the northward-heading component. The increase in speed towards the center of the channel, where advection is strongest, is clearly evident through an increased displacement between the ASTER and ETM positions. This is in agreement with earlier results (Watson & Robinson, 1990).

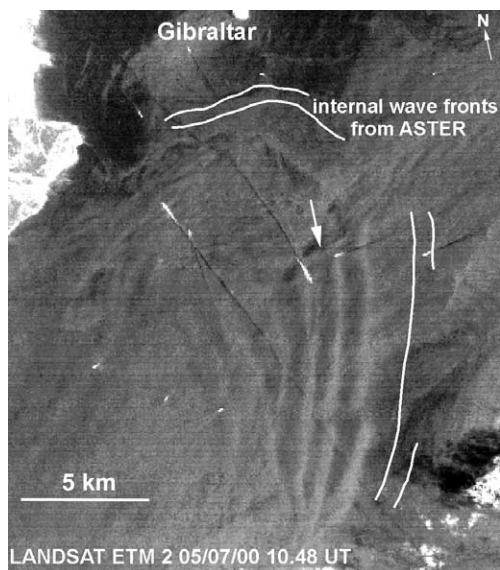


Fig. 5. A portion of a LANDSAT ETM image of the Strait of Gibraltar acquired in Channel 2 (green) at 10.48 UT on 5 July 2000, roughly 41 min prior to the TERRA overpass from which the ASTER data presented in Fig. 4 were gathered. The white lines indicate the later locations of the internal wave fronts, as deduced from the ASTER data. The speed of propagation increases toward the center of the channel up to a maximum value of 1.14 m s^{-1} .

Note that the oblique V-shaped disturbance discussed above in connection with the ASTER data can also be identified in the ETM image (one arm of this feature is marked with a white arrow), although at this earlier time it is considerably smaller in size. Comparison of the ASTER and ETM images shows that the apex moves westward (towards the Atlantic) at a speed of about 1.1 m s^{-1} whereas the downstream arms move slower the further they are from the apex and eventually acquire a speed of around 0.4 m s^{-1} . This disturbance is most likely related to the oblique wave pattern identified earlier in this area from space shuttle Sun glitter images and ascribed to the surface manifestation of internal waves generated through supercritical flow east of the narrowest part of the Strait (Farmer and Armi, 1986).

Within the 5 July 2000 ASTER stereo image pair, internal wave motion is best defined for an arm of this V-shaped disturbance where a speed of 1.1 m s^{-1} , equivalent to a 4-pixel shift, can be deduced toward the apex. This is consistent with the motion derived from the ASTER-ETM combination. Elsewhere, differential displacements were identifiable in the upper left quadrant of Fig. 4, where the internal wave field traversed the large ship wake, but as the ship was then only about 1.5 km distant some remnant influence of its passage may have been present. However, notwithstanding the relatively high internal wave speeds involved in the Strait, derivation of a synoptic view of the motion based on a comparison of the nadir and back-looking views obtained by ASTER remains difficult for the reasons outlined above. There is a similar inability to clearly resolve the motion of internal waves within the Izu Shoto image exhibited as Fig. 2. As at Gibraltar, this is largely due to the problem of identifying correspondence between the two views of a stereo pair for features with ill-defined edges and shapes that depend to some extent on view angle. Higher spatial and radiometric resolutions will help to solve this problem but may not eradicate it completely, given the limited time interval between the scenes. Sharply defined features, such as slicks, represent much better targets from the point of view of surface motion determination.

The TIR image presented in Fig. 4d was derived from Channel 14 of the TIR subsystem. These data, in providing what is essentially a high-resolution view of sea surface temperature variation, complete the suite of quality remote sensing observations offered by ASTER. The image shows that a well-defined surface flow of warmer water passes northeastward in the image, gradually narrowing in width as it moves into the Mediterranean. It is readily apparent that the disappearance of the main internal waves from the images in the center-channel region (in the northeast quadrants of Fig. 4a–c) coincides with the sudden narrowing and presumably strengthening of the surface flow in that region. From the ETM data of Fig. 5, it is interesting that this region also supports the genesis of the V-shaped internal wave disturbances discussed above. Since the events here take place slightly to the east of the narrowest part of the Strait, future work could examine in more detail a possible

link with constricted supercritical flow as suggested by Farmer and Armi (1986).

6. Brief examples of other uses of ASTER stereo data in oceanography and limnology

6.1. Swell waves and bottom topography

As swell waves travel with speeds of order 10 m s^{-1} , they will traverse distances of order 1 km over the 55 s time interval separating an ASTER 3N–3B stereo pair. Such large spatial displacements can be readily measured by a system with a 15-m spatial resolution. However, the potential for monitoring waves by ASTER is tempered by the fact that swell is not regularly detected in the channel 3B slant view.

Consider, the data shown in Fig. 6, in which both channels 3N and 3B show swell waves of wavelength between about 150 and 200 m arriving at a coastal region close to Shimoda (34.67°N , 138.92°E), a town on the Izu peninsula of Japan. The images exhibited here are extracts from the same ASTER scene as that used for the Izu Shoto image of Fig. 2 (acquired at 01.39 UT, 10.39 JST on 19 June 2004) except that they cover a region slightly further to the north and refer to a region nearer to the center of the scene.

As is a frequently observed in the near-nadir view of channel 3N, incoming swell waves are clearly visible in Fig. 6a through the Sun glitter modulations they produce. However, the fact that swell waves also appear in the back-looking view of Fig. 6b is rather unusual and is the combined result of several factors. The first of these is that the gain levels in both channels 3N and 3B were, as stated earlier, switched to their “High” settings for this acquisition,

whereas for the requirements of land observation, “Normal” gains are typically used. This is of more immediate importance for channel 3B where, even with a Sun glitter contribution, the received signal strengths from water surfaces are generally lower. The second factor is that a positive sensor tilt angle of 5.73° in the sunward direction (i.e. to the left of the TERRA platform in descending mode) was adopted. For the date and time relevant to the acquisition, this resulted in the presence of Sun glitter, which plays a vital facilitating role, in both the nadir and slant images. Finally, the swell waves themselves were strong and appear particularly well defined in shallower water (though not exclusively so). The orientations of the waves may also have played a role in the imaging although a wide range of propagation directions is actually represented in the images.

In the bottom left hand corner of Fig. 6a, a submerged ledge of depth under 10 m juts out from the coast and ends in a series of rounded submerged rock protrusions. In keeping with some of the local Japanese names for this area, the sea condition here is often bumpy. With the tide running largely eastward, this confused sea state is well represented by a highly irregular pattern in the near-nadir Sun glitter shown in Fig. 6a. Specular reflections from tilted surfaces developing over a range of spatial scales presumably make up the local glitter radiance. In addition, refraction of the incoming swell is particularly evident along a sharply defined boundary that marks the transition from deeper to shallower water. Further east, a dark region resembling a distorted triangle represents a zone of enhanced small-scale surface roughness, similar to that observed near the internal waves of Fig. 2. Enhanced Sun glitter from the swell in the small embayment to the north is likely due to reflection from the tilted backs of the swell waves, which are locally

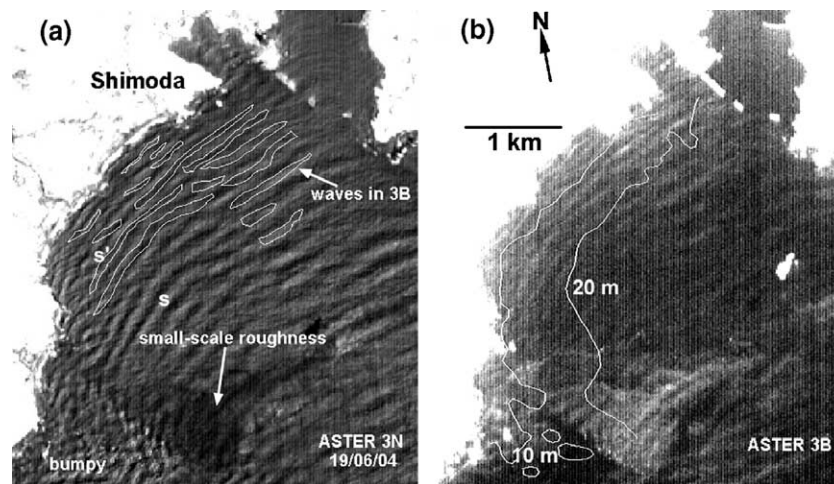


Fig. 6. (a) Swell waves of wavelength between about 150 and 200 m arrive at a coastal region close to Shimoda, Japan (34.67°N , 138.92°E) in this Channel 3N figure. The waves are visible through the variations they produce in Sun glitter. These data are extracts from a scene of the Izu Shoto region acquired by ASTER on 19 June 2004 at 01.39 UT (10.39 am JST) and discussed in connection with Fig. 2. Wave profiles deduced from the corresponding Channel 3B slant view of (b) are outlined in white. The wave crest labeled as “s” propagates to location “s’” over the 55 s separating the near-nadir and back-looking images, assuming an average speed of 12.75 m s^{-1} and a uniform depth variation. (b) The Channel 3B extract corresponding to the data shown in (a). Here fainter representations of the swell waves are visible through the Sun glitter modulation they cause. The 10-m and 20-m bathymetric contours are outlined in white.

smooth (low small-scale surface roughness), whereas the rougher leading faces of the waves appear dark.

In contrast to the near-nadir situation, the slant view of Fig. 6b shows that little signal was received from the confused patch of sea in the bottom left of the image as it appears dark, except in the shallowest regions. This indicates a meager contribution from larger-scale tilted facets and hence an inability to meet the more stringent requirement for specular reflection ($\beta_{N,sg}=6.55^\circ$ near nadir whereas $\beta_{B,sg}=20.26^\circ$ at slant) in the absence of small-scale surface roughness. When the latter is present, as in the distorted triangular region further to the east or on the leading faces of the swell waves, then higher signal strengths are recorded in the slant view. A useful test of the above interpretation would employ accurate modeling of wave propagation in an area of well-defined bottom topography in order to uncover the precise spatial relation between the near-nadir and back-looking intensity in images of the swell waves. As a first step in this direction, the profile of waves observed in the Channel 3B back-looking view of Fig. 6b are reproduced in outline in Fig. 6a. To give an indication of the spatial displacements involved, the wave crest labeled as “s” would propagate to location “s’” over the 55 s separating the two images, assuming an average speed of 12.75 m s^{-1} and a uniform depth variation.

6.2. Suspended sediment transport

Images derived from the ASTER 3B slant view are often quite effective at showing the presence of suspended sediment in surface waters. This capability arises from the fact that backscatter emanating from sediment-rich water can have a relatively large effect on the overall radiance

recorded in this channel, particularly when, for fairly smooth surfaces such as lakes, the Sun glitter contribution is small. As a result, the slant view can be useful in studying estuarine discharge, the coastal confinement of plumes or variations in water properties at frontal boundaries. In some cases, the nadir view of a sediment plume can be completely masked by strong reflections from regions of Sun glitter, so that the back-looking view then becomes the only means of determining its shape and location.

To illustrate this, Fig. 7a and b show extracts from a level 1A ASTER stereo pair covering the north coast of Siling Co, the second largest of central Tibet’s many lakes. This body of water, which lies at an altitude of 4530 m, covers an area of 1628 km^2 and has a relatively high mean salinity of 18 g l^{-1} . The turbidity of the lake is greatly influenced by the large Tsakya Tsangpo river which discharges into a small estuarine region at the north end of the lake. The views presented in Fig. 7a and b show this estuarine region as imaged by ASTER on 14 August 2001, with the river visible on the top right-hand corner. Different levels of contrast enhancement have been used in the upper and lower sections of these data in order to bring out the relevant details and hence both images are banded midway.

The most recent discharge plume extends into the central part of the embayment and displays lateral instability and an anti-clockwise gyre that marks the leading edge. Under roughly the same levels of contrast enhancement in the upper sections, the 3N nadir and 3B back-looking views of this young plume offer a generally similar depiction (no differential displacement could be reliably identified) but it is noticeable that the slant view is better able to pick out regions of relatively low sediment concentration. Further south, the nadir view receives strong Sun glitter that masks the path followed by the plume. In contrast, with Sun glitter

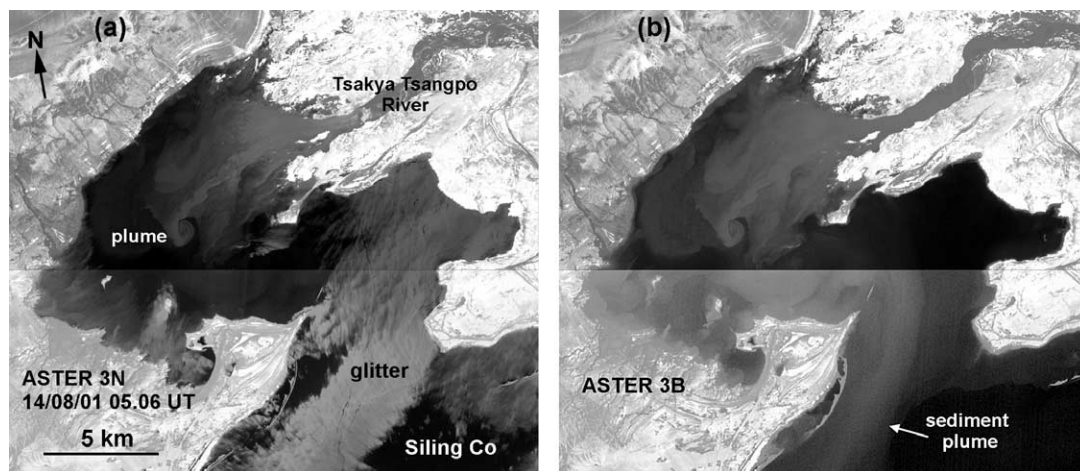


Fig. 7. (a) The channel 3N (near-infrared) image of the northern region of lake Siling Co, central Tibet, acquired by ASTER at 05.06 UT on 14 August 2001. The estuary of the river Tsakya Tsangpo is visible on the north of the image, with the river itself visible on the top right-hand corner. Different levels of contrast enhancement have been used in the top and bottom sections in order to emphasize the relevant details and hence the data are banded midway. Note that this nadir image contains extensive regions of Sun glitter that mask the path of the sediment-laden turbidity plume from the river. (b) As bright Sun glitter is largely absent from this corresponding channel 3B (near-infrared) back-looking view, the path of the sediment-rich water can be effectively tracked. The turbidity plume drifts out of the estuary and turns sharply southwestward where it drifts alongshore within the shallower coastal waters.

largely absent in the back-looking view of Fig. 7b, the track of the sediment-rich water can be identified in its entirety. The plume flows out of the estuary, turns sharply southwestward and then continues to drift in this direction within the shallower coastal waters.

6.3. Marine traffic monitoring and ship wakes

Fig. 8a represents a magnified version of an extract from the northwest portion of Fig. 4a and depicts a ship wake that traverses the internal wave field in the Gibraltar Strait. The corresponding close-up from channel 3B, acquired after a 55-s time interval, is given in Fig. 8b. Comparison of these ASTER images offers a straightforward means of monitoring ship traffic – here it shows that the vessel creating this extensive wake was traveling roughly southwestward at a speed of about 31 knots at the time of image acquisition. Similarly, a largely eastward flow at a speed of about 1.3 m s^{-1} can be deduced from the relative displacement of newly-formed wake in the two images.

For the nadir views, the turbulent wake is clearly visible as a dark line in which Sun glitter is suppressed. In addition, a similar but considerably fainter wake (less suppression) originates from the starboard side of the vessel. In terms of surface roughness, as expressed earlier through the mean square surface slope parameter, the situation for the main wake closely parallels that of the dark “trough” regions of the internal wave field shown in Fig. 4, in which the derived value of $\sigma_{\text{TW}}^2 (=0.0179)$ was indicative of locally smoother water. Note that the appearance of the wake here stands in complete contrast to the bright ship wake observed in the Izu Shoto image of Fig. 2. This reversal finds a natural explanation in the differing imaging geometries, as has been discussed above.

On encountering an internal wave “trough” the main turbulent wake is slightly extended in the transverse direction. Both the cusp and transverse waves within the

Kelvin envelope (Hennings et al., 1999) are well-defined and persist for many kilometers. Careful inspection of the data shows that the cusp-wave pattern appears to be disturbed by the presence of the internal waves, particularly in the vicinity of the strongest wave of the group where the cusp waves seem to undergo refraction caused, presumably, by the local surface current shear. An interesting aspect of the channel 3B slant view of Fig. 8b is the absence of both cusp and transverse waves. This is surprising, given the large amplitudes and range of orientations of the cusp waves but is consistent with the earlier discussion of swell waves and bottom topography. The main turbulent wake is, however, clearly visible as a dark line in the vicinity of the internal waves as there the local surface roughness is enhanced on both sides of the calmer wake. This is particularly so to the northeast of the wake. Beyond the region of the internal waves, the wake becomes fainter as it blends into the ambient background. The smaller wake from the starboard side of the ship now appears brighter than the main wake, consistent with a slightly higher remnant surface roughness.

7. Summary and Discussion

The aim of this article has been to demonstrate that a space-borne stereo viewing capability, of the type employed by ASTER, represents a new tool of considerable potential in the monitoring of coastal zone and lake environments. An important aspect of the stereo system is its ability to measure surface displacements that take place during the time interval between the nadir and back-looking views of the stereo pair. This forms the basis of a method for measuring surface current, wave propagation, ship motion, and wind velocity at cloud height. In addition, the stereo technique highlights the key role of viewing geometry in the imaging of oceanographic phenomena such as internal waves and suspended sediment transport. Within a simple theoretical

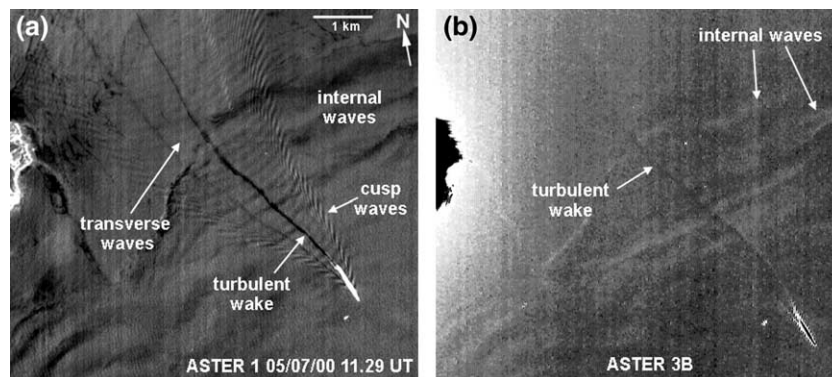


Fig. 8. (a) A magnified version of the large ship and its associated wake extracted from the northwest of the channel 1 (green) nadir data of Fig. 4a. The turbulent wake is clearly visible as a dark line in which Sun glitter is suppressed. In addition, a similar but considerably fainter wake originates from the starboard side of the vessel. Both cusp and transverse waves are also well-defined and extensive. The turbulent wake and the cusp waves are modified by the presence of the internal waves. (b) A close-up extracted from the VNIR time-delayed back-looking view (channel 3B, near infrared) of Fig. 4c that corresponds spatially to Fig. 5a. Comparison of these figures shows that the vessel was traveling roughly southwestward at a speed of about 31 knots at the time of the image acquisition. Similarly, an eastward flow at a speed of about 1.3 m s^{-1} can be deduced from the relative displacement of newly formed wake in the two images.

approach, it is also possible to make rough estimates of the mean square surface slope based on a ratio of the relative radiances measured in the nadir and back-looking views. In presenting the case for the stereo view, a number of applications in lake and marine settings have been discussed and in several of these the ASTER instrument suite provides a space-borne remote-sensing capability that is currently unrivalled.

As the ASTER stereo system was originally designed for use in land-based applications it is not ideally configured for the observation of water bodies. An idealized stereo imaging device, which could be dedicated to ocean observation, would require several key features. Crucially, it would need to operate at tilted viewing angles that enable it to gather Sun glitter images on a consistent basis. In addition, stereo operation at high radiometric sensitivity would be required for the slant views. Further, the use of a higher spatial resolution (relative to the 15 m offered by ASTER) would greatly improve the operational range and accuracy of surface velocity determinations. The acquisition of ocean Sun glitter images from front, nadir and back views would represent an additional improvement. It may be more appropriate to use extra wavelength bands centered on (visible) blue and green, rather than solely on near infrared as with ASTER, so that the sensor could return useful oceanographic information even if operated outside the Sun-glitter regime. Finally, contemporaneous measurement of marine surface wind by a dedicated instrument (such as a microwave scatterometer) would be a further useful addition.

Given that the availability of ASTER data has, through serendipity, led to the development of this new vista of stereo observation of lakes and coastal zones from space, in the short term it may be prudent to invest time in an aircraft-based campaign in order to determine an optimum configuration for the stereo observation of water bodies. In addition, theoretical work and further comparative studies using ASTER stereo views, SAR imagery and LANDSAT ETM data are required to improve the interpretation of the images obtained from this new source. Data from the forthcoming Advanced Land Observing Satellite (ALOS) will also be of value. This spacecraft will carry PRISM (the Panchromatic Remote-sensing Instrument for Stereo Mapping), which will gather forward, nadir and backward views at a spatial resolution of 2.5 m.

Acknowledgements

I acknowledge the assistance of staff at both Nagoya and Kyoto Universities. In particular, I thank Professors S.R. Wallis, Y. Yamaguchi, T. Awaji and S. Yoden for their support to this research. The Japanese Earth Remote Sensing and Data Acquisition Center (ERSDAC) supplied the ASTER imagery used here. Navigational charts and HF radar surface current observations were kindly supplied by the Japan Coast Guard. I received helpful advice on weather

and tidal conditions at Gibraltar from the Principal Officer of the Meteorological Office, Gibraltar. The LANDSAT ETM data used here were provided by EURIMAGE.

This work was initiated while the author was in receipt of a Visiting Professorship from Nagoya University and completed under the Kyoto University Center of Excellence (COE) plan for Active Geosphere Investigations in the 21st Century (KAGI21), a program supported by the Japanese Ministry of Education, Culture, Sports, Science and Technology (MEXT).

References

- Abrams, M., Hook, S. J., & Ramachandran, B. (2002). *ASTER users handbook, version 2*.
- Apel, J. R., Byrne, H. M., Proni, J. R., & Charnell, R. L. (1975). Observation of oceanic internal and surface waves from the earth resources technology satellite. *Journal of Geophysical Research*, *80*, 865–881.
- Barrick, D. E., Evans, M. W., & Weber, B. L. (1977). Ocean surface currents mapped by radar. *Science*, *198*(4313), 138–144.
- Brandt, P., Alpers, W., & Backhaus, J. (1996). Study of the generation and propagation of internal waves in the Strait of Gibraltar using a numerical model and synthetic aperture radar images of the European ERS 1 satellite. *Journal of Geophysical Research*, *101*, 14237–14252.
- Crombie, D. D. (1955). Doppler spectrum of sea echo at 13.56 Mc/s. *Nature*, *175*(4459), 681–682.
- Cox, C., & Munk, W. H. (1954). The measurement of the roughness of the sea surface from photographs of the sun's glitter. *Journal of the Optical Society of America*, *44*, 838–850.
- da Silva, J. C. B., Correia, S., Ermakov, S. A., Sergievskaya, I. A., & Robinson, I. S. (2004). Synergy of MERIS/ASAR for observing marine film slicks and small scale processes. *Proc. MERIS User Workshop, Frascati, Italy, 1013 November, 2003 (ESA SP-549, May 2004)*.
- Farmer, D. M., & Armi, L. (1986). Maximal two-layer exchange over a sill and through the combination of a sill and contraction with barotropic flow. *Journal of Fluid Mechanics*, *164*, 53–76.
- Hennings, I., Matthews, J. P., & Metzner, M. (1994). Sun glitter radiance and radar cross-section modulations of the sea bed. *Journal of Geophysical Research*, *99*(C8), 16303–16326.
- Hennings, I., Romeiser, R., Alpers, W., & Viola, A. (1999). Radar imaging of Kelvin arms of ship wakes. *International Journal of Remote Sensing*, *20*(13), 2519–2543.
- Khattak, S., Vaughan, R. A., & Cracknell, A. P. (1991). Sun glint and its observation in AVHRR data. *Remote Sensing of Environment*, *37*, 101.
- Kinoshita, H., Yoritaka, H., Takashiba, T., & Ito, T. (2004). Validation of ocean current observation with high-frequency radar. *Report of Hydrographic and Oceanographic Researches*, *40*, 93–101 (in Japanese).
- Liu, Y., Yan, X. -H., Liu, W. T., & Hwang, P. A. (1997). The probability density function of ocean surface slopes and its effect on radar backscatter. *Journal of Geophysical Research*, *27*, 782–797.
- Matthews, J. P., Fox, A. D., & Prandle, D. (1993). Radar observations of an along-front jet and transverse flow convergence associated with a North Sea front. *Continental Shelf Research*, *13*(1), 109–130.
- Matthews, J. P., Wallis, S. R., & Yamaguchi, Y. (2004). ASTER views a high altitude Tibetan lake in stereo. *EOS*, *85*(43), 435.
- Matthews, J. P., Wismann, V., Lwiza, K., Romeiser, R., Hennings, I., & de Loo, G. P. (1997). The observation of the surface roughness characteristics of the Rhine plume frontal boundaries by simultaneous Airborne Thematic Mapper and multifrequency helicopter-borne radar scatterometer. *International Journal of Remote Sensing*, *18*(9), 2021–2033.
- Melsheimer, C., & Kwok, L.K. (2001). Sun glitter in SPOT images and the visibility of oceanic phenomena. *Paper presented at the 22nd Asian Conference on Remote Sensing, 59 November 2001, Singapore*.

- Mohan, M., & Chauhan, P. (2001). Simulations for optimal payload tilt to avoid sunglint in IRS-P4 Ocean Colour Monitor (OCM) data around the Indian subcontinent. *International Journal of Remote Sensing*, 22(1), 185–190.
- Munk, W., Armi, L., Fischer, K., & Zachariasen, F. (2000). Spirals on the sea. *Proceedings of the Royal Society of London. Series A*(456), 1217–1280.
- Prandle, D., & Matthews, J. P. (1990). The dynamics of nearshore surface currents generated by tides, wind and horizontal density gradients. *Continental Shelf Research*, 7(10), 665–681.
- Prandle, D., & Ryder, D. K. (1985). Measurement of surface currents in Liverpool Bay by high frequency radar. *Nature*, 315, 128–131.
- Sakuno, M., & Matsunaga, T. (2002). Preliminary study for monitoring SST and turbidity using ASTER data in Hiroshima Bay, *Presented at ASTER Science team meeting, ASTER workshop, Aoyama TEPIA, Tokyo, 2226, May 2002*.
- Takasaki, K., Sugimura, T., & Tanaka, S. (1994). Speed vector measurement of moving objects using JERS-1/OPS data. *Journal of the Remote Sensing Society of Japan*, 14(3), 213–219 (in Japanese, with English Abstract).
- Watson, G., & Robinson, I. (1990). A study of internal wave propagation in the Strait of Gibraltar using shore-based marine radar images. *Journal of Physical Oceanography*, 20, 374–395.
- Yamaguchi, Y., Kahle, A. B., Tsu, H., Kawakami, T., & Pniel, M. (1998). Overview of Advanced Spaceborne Thermal Emission and Reflection Radiometer (ASTER). *IEEE Transactions on Geoscience and Remote Sensing*, 36(4), 1062–1071.
- Zeisse, C. R. (1995). Radiance of the ocean horizon. *Journal of the Optical Society of America A*, 12(9), 2022–2030.
- Zheng, Q., Klemas, V., & Xiao-Hai, Y. (1995). Dynamic interpretation of space shuttle photographs: deepwater internal waves in the western equatorial Indian Ocean. *Journal of Geophysical Research*, 100(C2), 2579–2590.